GT2014-25967

DEVELOPMENT OF A PRESSURE-BASED COUPLED CFD SOLVER FOR TURBULENT AND COMPRESSIBLE FLOWS IN TURBOMACHINERY APPLICATIONS

Luca Mangani *

University of Applied Sciences Luzern Technik & Architektur Technikumstrasse 21, 6048 Horw, Switzerland luca.mangani@hslu.ch

Marwan Darwish, Fadl Moukalled

American University of Beirut P.O.Box 11-0236 (Department) Riad El-Solh Beirut 1107 2020 Lebanon

ABSTRACT

In this paper we present a fully coupled algorithm for the resolution of compressible flows at all speed. The pressure-velocity coupling at the heart of the Navier Stokes equations is accomplished by deriving a pressure equation in similar fashion to what is done in the segregated SIMPLE algorithm except that the influence of the velocity fields is treated implicitly. In a similar way, the assembly of the momentum equations is modified to treat the pressure gradient implicitly. The resulting extended system of equations, now formed of matrix coefficients that couples the momentum and pressure equations, is solved using an algebraic multigrid solver.

The performance of the coupled approach and the improved efficiency of the novel developed code was validated comparing results with experimental and numerical data available from reference literature test cases as well as with segregated solver as exemplified by the SIMPLE algorithm. Moreover the reference geometries considered in the validation process cover the typical aerodynamics applications in gas turbine analysis and design, considering Euler to turbulent flow problems and clearly indicating the substantial improvements in terms of computational cost and robustness.

NOMENCLATURE

a coefficients in the discretized equation $[kg s^{-1}]$

b	general source term	[-]
d	space vector joining the grid points P and F	[m]
D	discretized laplacian operator	$[s k g^{-1}]$
k	thermal conductivity	$[W m^{-2} K^{-1}]$
g	geometric interpolation factor	[-]
H	total Enthalpy	$[m^2 s^{-2}]$
\dot{m}_f	mass flow rate at control volume face f	$[kg s^{-1}]^{'}$ $[kg m^{-1} s^{-2}]$
p	pressure	$[kg m^{-1} s^{-2}]$
S	surface vector	$[m^2]$
u, v, w	velocity components in x-,y- and z-directions, respectively	$[m s^{-1}]$
u	velocity vector	$[m s^{-1}]$
Ω	angular velocity	$[s^{-1}]$

Subscripts Greeks

		f	refers to control volume face
ρ	fluid density	NB	refers to neighbors cells
μ	dynamic viscosity	P	diagonal cell
		x, y, z	refers to x, y and w directions

INTRODUCTION

OpenFOAM® is an finite volume based open source CFD toolbox that can be used for the resolution of a wide range of flow problems which solves the Navier-Stokes equations in a segregated fashion. Over the past few years its popularity has increased substantially not only in the academic community but also in a number of industries. The main drivers behind this increased adoption rate has been the full source code access that allows for complete "customization", in addition to the low running cost especially when running large number of "seats" in parallel without the usual associated licensing costs

^{*}Address all correspondence to this author.

of commercial CFD software.

However in some industries, such as (thermal) turbomachinery related ones, the adoption of OpenFOAM® is still lagging. A critical issue has been the inability of the OpenFOAM® core solvers to robustly resolve this class of problems, characterized by complex compressible flows in complex rotating geometries. In fact, the basic built-in solvers for highly compressible flows cannot yet resolve industrial viscous transonic flows, i.e. the complete Mach number regime, present in industrial turbomachinery applications. This state of affairs and the continuing interest in these industries to be benefit from the advantages of an open source code, is providing a high incentive to remedy this weakness.

It is worth noting that a similar effort expanded over the last decade by one of the authors [1], extended the ability of OpenFOAM® to robustly and efficiently address a range of all-speed flows resulting in improved accuracy to levels similar to commercial codes, for industrial turbomachinery applications [2, 3], for internal and external aero-thermal flows [4], for conjugate heat transfer with fluid structure interaction with/without film cooling [5,6] and for high pressure centrifugal compressors [7,8]. Nevertheless an improved computational efficiency still has to be addressed and the approach adopted in this work is through the development and implementation of a fully coupled pressure based method.

The context of this approach follows the decades of development that expanded the application of the pressure-based SIMPLE family [9] of algorithms used in the solution of the Navier-Stokes equations, from the original staggered structured grid, single fluid incompressible flow applications [10–12] to an unstructured collocated framework that is applicable to a wide range of fluid flow problems, from single-phase incompressible [13] and compressible [14], to multi-phase [15]. At the same time many issues of contention such as the choice of primitive variables (density-based [16] versus pressure-based [15, 17]), the type of variable arrangement (staggered versus collocated arrangement [18]) are now either better understood or resolved.

A new issue that has continues to be revisited is the segregated vs. coupled approach [19]. What is forcing this issue is the effect of increasing problem size on the performance of the current generation of segregated pressure-algorithms, which continue to suffer from a breakdown in convergence rate when applied to the solution of large scale problems. This is mainly due to the weak resolution of the Navier-Stokes equations velocity-pressure coupling using SIMPLE family algorithms, which in compressible flows extends to the density and energy fields. Addressing this weakness can be achieved with numerics that reflect the strong coupling present in the NS equations. This is accomplished by solving the system of discretized equations simultaneously, thus ensuring that the coupling of the equations is preserved during each solution step. This stands in contrast to the segregated approach used in the SIMPLE algorithms, where

the equations are solved sequentially.

As described in [20] this coupled approach but only with a proper linearization of the Navier-Stokes equations is actually used in the density-based algorithms, where continuity, momentum and energy equations are solved as one system of equations. It is also worth noting that the Imperial College group originator of the SIMPLE algorithm had started their work on a coupled pressure-based solver rather than on a segregated one. However the coupled algorithm, known as SIVA [21], was overshadowed by the SIMPLE algorithm that combined low memory requirement with coding simplicity, two substantial advantages given the state of computer technology at that time.

The objective of the work presented in this paper is to show the extended capabilities of that can be achieved by combining strongly coupled numerics with the OpenFOAM[®] open-source software environment. Benefiting as we do from the framework architectural strengths while delivering a more robust solution.

This in the view of the authors will allow the OpenFOAM[®] toolbox to grow into a complete CFD suite for the steady and unsteady analyses for turbomachinery applications.

In what follows the developed coupling procedure is presented along with some implementation details. The resulting algorithm is then assessed by solving test-case problems with comparison to an OpenFOAM® solver based on the segregated SIMPLE algorithm. Transonic and supersonic flow results are also reported in order to show the capabilities of the shock-capturing technique together with the coupled acceleration.

NUMERICAL APPROACH Coupled Algorithm

The convergence of the segregated SIMPLE algorithm is highly affected by the explicit treatment of the pressure gradient in the momentum equation and the velocity field in the continuity equation. Treating both terms in an implicit manner is in essence the aim of any coupled algorithm. This is achieved here by coupling the momentum and the pressure-form of the continuity equation through a set of coefficients that represent the mutual influence of continuity and momentum on the pressure and the velocity fields.

An important aspect of this procedure is the choice of the primitive variables that plays a key role for the corresponding system during the implicit discretization. Starting from the incompressible formulation of the Navier-Stokes equations, the discretization by finite volume scheme leads to a system matrix which takes the form of the following saddle point problem, [22].

$$\begin{bmatrix} A & B \\ B^T & 0 \end{bmatrix} \begin{bmatrix} \mathbf{v} \\ p \end{bmatrix} = \begin{bmatrix} f \\ 0 \end{bmatrix} \tag{1}$$

where A is a convection-diffusion type matrix, B and B^T are the discrete gradient and divergence matrices.

To avoid forming a saddle-point matrix that result from a direct discretization of the Navier-Stokes equations, a special treatment is used for the pressure field, this basically takes the form of a reformulation of the continuity equation into a constraint pressure equation that enforces mass conservation on the velocity fields. This procedure is basically at the core of the SIMPLE family of algorithms [23] originally developed for staggered grids. For a collocated grid arrangement, a special velocity interpolation, the Rhie-Chow interpolation, is used to overcome any checker boarding of the pressure field [24]. The distinguishing feature of the coupled OpenFOAM® based solver is the fully implicit algorithm that is used to resolve the velocity pressure coupling that arise from the Navier-Stokes equations. The algorithm was originally presented by Darwish et. [25], and is implemented within the OpenFOAM® framework with minor modifications. Also the implementation of the turbulence model is enhanced to allow consistent behavior in combination with the coupled solver. In what follows the details of the discretization procedure for the momentum and continuity equations will be discretized, this will include details on the resolution of the coupling between these two equations. Then the discretization of the Energy equation is presented along with details related to the treatment of the Moving Reference frame and the solution of the resulting systems of equations.

Discretisation of the momentum equations

The steady state momentum equations are first reformulated in integral form to yield,

$$\oint_{S} (\rho \mathbf{u} \mathbf{u})_{f} \cdot \mathbf{n} dS = -\oint_{S} \mathbf{n} p_{f} dS + \oint_{S} \left[\mathbf{n} \cdot \left(\mu_{eff} (\nabla \mathbf{u})_{f} \right) \right] dS \quad (2)$$

Using the mid-point rule the surface fluxes are Integrated over the discrete faces of the polygonal elements to yield

$$\sum_{faces} \dot{V}_f \mathbf{u}_f + \sum_{faces} \mathbf{S}_f p_f - \frac{1}{\rho} \sum_{faces} \mathbf{S}_f \cdot (\mu_{eff} \nabla \mathbf{u}_f) = 0$$
 (3)

The convection term in equation (2) is linearised by computing the convecting flux ($\dot{V}_f = \rho_f \mathbf{u}_f \cdot \mathbf{n} \, dS$) using previous iteration values. Starting with the first term (Convection), and using a first order upwind discretization we get

$$a_C^{uu} = |\dot{V}_f^n, 0|$$
 $a_{NB}^{uu} = -|-\dot{V}_f^n, 0|$
 $a_C^{vv} = |\dot{V}_f^n, 0|$ $a_{NB}^{vv} = -|-\dot{V}_f^n, 0|$
 $a_C^{ww} = |\dot{V}_f^n, 0|$ $a_{NB}^{ww} = -|-\dot{V}_f^n, 0|$

where n and hereafter indicates a value from the previous iteration. For the second term (pressure gradient) a linear interpolation is used to express the face pressure in terms of the two cell values straddling the face under consideration. With g_f representing the interpolation weight, we get

$$a_C^{up} = S_{f_x} g_f$$
 $a_{NB}^{up} = S_{f_x} (1 - g_f)$
 $a_C^{vp} = S_{f_y} g_f$ $a_{NB}^{vp} = S_{f_y} (1 - g_f)$
 $a_C^{wp} = S_{f_z} g_f$ $a_{NB}^{wp} = S_{f_z} (1 - g_f)$

The third term (stress) is re-written in terms of an implicit orthogonal component and an explicit non-orthogonal component following the treatment

$$\mathbf{S}_{f} \cdot \left(\mu_{eff} \left(\nabla \mathbf{u}\right)_{f}\right) = \mu_{eff} \frac{\mathbf{S}_{f} \cdot \mathbf{S}_{f}}{\mathbf{d} \cdot \mathbf{S}_{f}} \left(\mathbf{u}_{NB} - \mathbf{u}_{C}\right) + \mu_{eff} \underbrace{\left(\mathbf{S}_{f} - \frac{\mathbf{S}_{f} \cdot \mathbf{S}_{f}}{\mathbf{S}_{f} \cdot \mathbf{d}} \mathbf{d}\right)}_{\mathbf{T}} \cdot \overline{\nabla \mathbf{u}_{f}}$$
(4)

The orthogonal part in equation(4) is written into the coefficients,

$$\begin{aligned} a_C^{uu} &= \mu_{eff}^n \frac{\mathbf{S}_f \cdot \mathbf{S}_f}{\mathbf{d} \cdot \mathbf{S}_f} & a_{NB}^{uu} &= -\mu_{eff}^n \frac{\mathbf{S}_f \cdot \mathbf{S}_f}{\mathbf{d} \cdot \mathbf{S}_f} \\ a_C^{vv} &= \mu_{eff}^n \frac{\mathbf{S}_f \cdot \mathbf{S}_f}{\mathbf{d} \cdot \mathbf{S}_f} & a_{NB}^{vv} &= -\mu_{eff}^n \frac{\mathbf{S}_f \cdot \mathbf{S}_f}{\mathbf{d} \cdot \mathbf{S}_f} \\ a_C^{ww} &= \mu_{eff}^n \frac{\mathbf{S}_f \cdot \mathbf{S}_f}{\mathbf{d} \cdot \mathbf{S}_f} & a_{NB}^{uw} &= -\mu_{eff}^n \frac{\mathbf{S}_f \cdot \mathbf{S}_f}{\mathbf{d} \cdot \mathbf{S}_f} \end{aligned}$$

while the non-orthogonal part is treted explicitly and written into the right hand side. Thus we get

$$b_{C}^{u} = \mu_{eff}^{n} \left(T_{x} \frac{\overline{\partial u}^{n}}{\partial x_{f}} + T_{y} \frac{\overline{\partial u}^{n}}{\partial y_{f}} + T_{z} \frac{\overline{\partial u}^{n}}{\partial z} \right)$$

$$b_{C}^{v} = \mu_{eff}^{n} \left(T_{x} \frac{\overline{\partial v}^{n}}{\partial x_{f}} + T_{y} \frac{\overline{\partial v}^{n}}{\partial y_{f}} + T_{z} \frac{\overline{\partial v}^{n}}{\partial z_{f}} \right)$$

$$b_{C}^{w} = \mu_{eff}^{n} \left(T_{x} \frac{\overline{\partial w}^{n}}{\partial x_{f}} + T_{y} \frac{\overline{\partial w}^{n}}{\partial y_{f}} + T_{z} \frac{\overline{\partial w}^{n}}{\partial z_{f}} \right)$$

The gradient $\overline{\nabla \mathbf{u}_f}$ is evaluated from the previous field values.

The discretized momentum equation can now be written as.

$$\begin{bmatrix} |\dot{V}_{f},0| + \mu_{eff}^{n} \frac{\mathbf{S}_{f} \cdot \mathbf{S}_{f}}{\mathbf{d} \cdot \mathbf{S}_{f}} & 0 & 0 \\ 0 & |\dot{V}_{f},0| + \mu_{eff}^{n} \frac{\mathbf{S}_{f} \cdot \mathbf{S}_{f}}{\mathbf{d} \cdot \mathbf{S}_{f}} & 0 \\ 0 & 0 & |\dot{V}_{f},0| + \mu_{eff}^{n} \frac{\mathbf{S}_{f} \cdot \mathbf{S}_{f}}{\mathbf{d} \cdot \mathbf{S}_{f}} \end{bmatrix} \cdot \begin{bmatrix} u_{C} \\ v_{C} \\ v_{C} \end{bmatrix}$$

$$+ \sum_{faces} \begin{bmatrix} |\dot{V}_{f},0| - \mu_{eff}^{n} \frac{\mathbf{S}_{f} \cdot \mathbf{S}_{f}}{\mathbf{d} \cdot \mathbf{S}_{f}} & 0 & 0 \\ 0 & |\dot{V}_{f},0| - \nu_{eff}^{n} \frac{\mathbf{S}_{f} \cdot \mathbf{S}_{f}}{\mathbf{d} \cdot \mathbf{S}_{f}} & 0 \\ 0 & 0 & |\dot{V}_{f},0| - \mu_{eff}^{n} \frac{\mathbf{S}_{f} \cdot \mathbf{S}_{f}}{\mathbf{d} \cdot \mathbf{S}_{f}} \end{bmatrix} \cdot \begin{bmatrix} u_{NB} \\ v_{NB} \\ v_{NB} \end{bmatrix}$$

$$+ V_{C} \nabla p_{C} = \begin{bmatrix} \mu_{eff}^{n} \left(T_{x} \frac{\overline{\partial u}}{\partial x_{f}}^{n} + T_{y} \frac{\overline{\partial u}}{\partial y_{f}}^{n} + T_{z} \frac{\overline{\partial u}}{\partial z_{f}}^{n} \right) \\ \mu_{eff}^{n} \left(T_{x} \frac{\overline{\partial u}}{\partial x_{f}}^{n} + T_{y} \frac{\overline{\partial v}}{\partial y_{f}}^{n} + T_{z} \frac{\overline{\partial v}}{\partial z_{f}}^{n} \right) \\ \mu_{eff}^{n} \left(T_{x} \frac{\overline{\partial w}}{\partial x_{f}}^{n} + T_{y} \frac{\overline{\partial w}}{\partial y_{f}}^{n} + T_{z} \frac{\overline{\partial w}}{\partial z_{f}}^{n} \right) \end{bmatrix}$$

$$(5)$$

Equation (5) can be written as,

$$\mathbf{a}_C \cdot \mathbf{u}_C + \sum_{faces} \mathbf{a}_{NB} \cdot \mathbf{u}_{NB} + V_C \nabla p_C = \mathbf{b}_C^{\mathbf{u}}$$
 (6)

or,

$$\mathbf{u}_C + \mathbf{a}_C^{-1} \cdot \mathbf{a}_{NB} \cdot \mathbf{u}_{NB} + \mathbf{a}_C^{-1} \cdot (V_C \nabla p_C) = \mathbf{a}_C^{-1} \cdot \mathbf{b}_C^{\mathbf{u}}$$
 (7)

Leading finally to the operator form of the discretized momentum equation.

$$\mathbf{u}_C + \mathbf{H}_C(\mathbf{u}) + \mathbf{D}_C \cdot \nabla p_C = \tilde{\mathbf{b}}_C^{\mathbf{u}}$$
 (8)

Discretizing the continuity equations

For compressible flows the mass conservation is enforced through the continuity equation using two mechanisms, for low mach number flows the velocity fields is mainly affected by the pressure gradient, for higher mach number flows density changes become the more significant factor. Obviously the pressure, density relation is also dependent on the temperature field via the equation of state,

$$p = \rho RT \tag{9}$$

For steady state the continuity equation (10) in integral form reads

$$\oint_{S} \rho \mathbf{u} \cdot \mathbf{n} \, d\mathbf{S} = 0 \tag{10}$$

Again integrating over the faces of our element yields

$$\sum_{faces} \rho \mathbf{u}_f \cdot S_f = 0 \tag{11}$$

Since both density and velocity are to be computed the above equation is linearized as

$$\sum_{faces} (\rho \mathbf{u}_f^n + \rho^n \mathbf{u}_f - \rho^n \mathbf{u}_f^n) \cdot S_f = 0$$
 (12)

In (12) \mathbf{u}_f represents the face value of the velocity field, in a staggered grid this would be obtained directly from the algebraic form of the momentum equations. In a collocated framework, the velocity at the face is obtained by reconstructing a pseudo momentum equation at the face. This is basically the function of the Rhie-Chow interpolation [24]. The reconstructed equivalent of the momentum equation is written as

$$\mathbf{u}_f + \mathbf{H}_f(\mathbf{u}) + \mathbf{D}_f \cdot \nabla p_f = \tilde{\mathbf{b}}_C^{\mathbf{u}}$$
 (13)

where the tensor $\mathbf{D}_f(\mathbf{u})$ at a cell face is interpolated from adjacent cells value of \mathbf{D} to the face.

$$\mathbf{D}_f(\mathbf{u}) \approx \overline{\mathbf{D}_f(\mathbf{u})} \tag{14}$$

and the $\mathbf{H}_f(u)$ -operator obtained by interpolation as

$$\mathbf{H}_f(\mathbf{u}) \approx \overline{\mathbf{H}_f(\mathbf{u})} \approx -\overline{\mathbf{u}_f} - \overline{\mathbf{D}_f \cdot \nabla p_f} + \overline{\tilde{\mathbf{b}}_C^{\mathbf{u}}}$$
 (15)

substituting (14) and (15) into (13) we get

$$\mathbf{u}_{f} - \overline{\mathbf{u}_{f}} - \overline{\mathbf{D}_{f} \cdot \nabla p_{f}} + \mathbf{D}_{f} \cdot \nabla p_{f} = \underbrace{\tilde{\mathbf{b}}_{C}^{\mathbf{u}} - \overline{\tilde{\mathbf{b}}_{C}^{\mathbf{u}}}}_{\approx 0}$$
(16)

or the more standard form

$$\mathbf{u}_f = \overline{\mathbf{u}_f} - \overline{\mathbf{D}_f} \cdot (\nabla p_f - \overline{\nabla p_f}) \tag{17}$$

The density ρ_f is replaced with p_f using the equation of state to yield

$$\rho_f = p_f / (RT^*) \tag{18}$$

substituting (18) and (17) into (10) we get our pressure equation as

$$\sum_{faces} \left(\mathbf{S}_{f} \cdot \mathbf{u}_{f} / (RT^{n}) p_{f} + \mathbf{S}_{f} \cdot \rho_{f}^{n} \left(\overline{\mathbf{u}}_{f} - \overline{\mathbf{D}_{f}} \cdot \left(\nabla p_{f} - \overline{\nabla p_{f}} \right) \right) \right)$$

$$= \mathbf{S}_{f} \cdot \mathbf{u}_{f}^{n} \rho_{f}^{n}$$
(19)

The velocity part of equation (19) yields the following implicit coefficients.

$$a_C^{pu} = \rho S_{f_x} (1 - g_f)$$
 $a_{NB}^{pu} = \rho S_{f_x} g_f$
 $a_C^{pv} = \rho S_{f_y} (1 - g_f)$ $a_{NB}^{pv} = \rho S_{f_y} g_f$
 $a_{NB}^{pw} = \rho S_{f_z} (1 - g_f)$ $a_{NB}^{pw} = \rho S_{f_z} g_f$

The implicit pressure gradient part is discretized similar to the viscous term of the continuity equations (3), the interpolated pressure gradient part is treated purely explicitly. Again sub-looping will lead to a converged solution of the system. Note that the Rhie-Chow diffusion part will not vanish completely for a converged solution since the terms are not discretized equally. However with decreasing mesh size the remainder tends to zero. Since the method is based on unstructured grids, the implicit pressure gradient has to be split into an implicit part along the line connecting two neighboring cell centers and a correction part that has to be evaluated explicitly,

$$-\mathbf{S}_{f} \cdot \overline{\mathbf{D}_{f}} \cdot \nabla p_{f} = -\frac{\mathbf{S}_{f} \cdot \overline{\mathbf{D}_{f}} \cdot \mathbf{S}_{f}}{\mathbf{d} \cdot \mathbf{S}_{f}} (p_{NB} - p_{C})$$

$$-\underbrace{\left(\mathbf{S}_{f} \cdot \overline{\mathbf{D}_{f}} - \frac{\mathbf{S}_{f} \cdot \overline{\mathbf{D}_{f}} \cdot \mathbf{S}_{f}}{\mathbf{d} \cdot \mathbf{S}_{f}} \mathbf{d}\right)}_{\mathbf{N}} \cdot \nabla p_{f}}$$
(20)

$$a_C^{pp} = \frac{\mathbf{S}_f \cdot \overline{\mathbf{D}_f} \cdot \mathbf{S}_f}{\mathbf{d} \cdot \mathbf{S}_f} \quad a_{NB}^{pp} = -\frac{\mathbf{S}_f \cdot \overline{\mathbf{D}_f} \cdot \mathbf{S}_f}{\mathbf{d} \cdot \mathbf{S}_f}$$
$$b_C^p = \mathbf{N} \cdot \overline{\nabla p_f}$$

The advection like term for the pressure provides the additional matrix elements coefficients

$$a_C^{pp} = a_C^{pp} + |(\mathbf{u}_f/(RT))^n, 0|$$
 $a_{NB}^{pp} = a_{NB}^{pp} - |-(\mathbf{u}_f/(RT))^n, 0|$

The explicit pressure gradient of equation (19) yields,

$$b_C^p = -\mathbf{S}_f \overline{\mathbf{D}_f} \cdot \overline{\nabla p_f}$$

A more detailed description of the laplacian discretization for unstructured, non-orthogonal, collocated grids is given by Muzaferija [26] and Ferziger [27]. The obtained discretized block coupled system of equations contains now extra-diagonal

elements, for both diagonal and off-diagonal block coefficients. For the sake of brevity the block coefficients are written down such that a surface integration over a cell is assumed, the cell C sharing its faces with neighboring cells NB. Like this, the block coefficients a_C are directly added to the diagonal block coefficient array, whereas the neighboring block coefficients a_{NB} are injected into the off-diagonal block coefficient arrays. Equation (21), shows the resulting block coefficient filling.

$$\begin{bmatrix} a_{C}^{uu} & a_{C}^{vv} & a_{C}^{uw} & a_{C}^{up} \\ a_{C}^{vu} & a_{C}^{vv} & a_{C}^{vw} & a_{C}^{vp} \\ a_{C}^{wu} & a_{C}^{vv} & a_{C}^{w} & a_{C}^{vp} \\ a_{C}^{wu} & a_{C}^{vv} & a_{C}^{vw} & a_{C}^{vp} \\ a_{C}^{vu} & a_{C}^{vv} & a_{C}^{vw} & a_{C}^{vp} \end{bmatrix} \cdot \begin{bmatrix} u_{C} \\ v_{C} \\ w_{C} \\ p_{C} \end{bmatrix} + \\ + \sum_{faces} \begin{bmatrix} a_{NB}^{uu} & a_{NB}^{uv} & a_{NB}^{uw} & a_{NB}^{uw} & a_{NB}^{vp} \\ a_{NB}^{vu} & a_{NB}^{vw} & a_{NB}^{vw} & a_{NB}^{vp} \\ a_{NB}^{vu} & a_{NB}^{vv} & a_{NB}^{vw} & a_{NB}^{vw} \end{bmatrix} = \begin{bmatrix} b_{C}^{u} \\ b_{C}^{v} \\ b_{C}^{v} \\ b_{C}^{v} \end{bmatrix}$$

$$(21)$$

Energy Equation

While density based coupled solvers [28] include the energy equation directly as part of the coupled system of momentum and density, our pressure based coupled algorithm does not, rather the conservation equation of the total enthalpy H is solved separately in a segregated manner. The reasons for this choice is that in the pressure-velocity coupling we are solving for primitive variables and not for conservative variables as for density based algorithm. In the pressure-based coupled solver the coupling between the energy and momentum equations can be treated through a Picard iteration approach and no approximate Riemann solver is needed, i.e. [29] for higher order convection reconstruction. rather NVD or TVD schemes [30] can be used. Moreover the use of total enthalpy equation shown below leads to the standard convection diffusion equation formulation where the viscous heating remains the only main term of coupling with the momentum equation.

$$\nabla \cdot (\rho \mathbf{u} H) = -\nabla \cdot (k(\nabla T)) + \nabla \cdot (\mathbf{R} \cdot \mathbf{u}) \tag{22}$$

where the term $\nabla \cdot (\mathbf{R} \cdot \mathbf{u})$ represents the work due to viscous stresses also named viscous work term or viscous heating.

Finally a segregated formulation of the energy equation allows the use of specific solving times or relaxation for the solid domains with an improved acceleration of the convergence for applications involving conjugate heat transfer [6] .

Moving Reference of Frame

In a rotating reference frame with constant angular velocity $(\dot{\Omega}=0)$ the Navier-Stokes equations for steady flows can be reformulated in terms of the stationary, or absolute, velocity [31]

yielding

$$\nabla \cdot (\rho \mathbf{u_r} \mathbf{u}) + \rho \Omega \times \mathbf{u} = -\nabla p + \nabla \cdot (\mu_{eff}(\nabla \mathbf{u}))$$
 (23)

Taking advantage of the new coupled framework, the rotational term $\Omega \times \mathbf{u}$, is discretized implicitly by integrating it over a control volume and adding the resulting coefficient to the diagonal matrix:

$$\begin{array}{ll} a^{uv}_{C,rot} = -\rho \Omega_z \Delta V & a^{uw}_{C,rot} = \ \rho \Omega_y \Delta V \\ a^{vu}_{C,rot} = \ \rho \Omega_z \Delta V & a^{vw}_{C,rot} = -\rho \Omega_x \Delta V \\ a^{wu}_{C,rot} = -\rho \Omega_y \Delta V & a^{wv}_{C,rot} = \ \rho \Omega_x \Delta V \end{array}$$

This implicit treatment of the non-inertial term was found to improve performance and robustness in the code as compared to the standard procedure that lumps the extra terms into the source term.

Efficient Implementation of the Coupled Solver

The system of equations resulting from the coupled discretization has a block matrix structure and is for a similar mesh 16 times larger than that obtained from segregated discretization for one variable. It is thus essential to use an efficient and highly scalable iterative solver. A combination of multigrid with an iterative solver with good smoothing properties was found to provide these characteristics.

Multi-grid methods introduced by Federenko [32], Poussin [33] and later re-discovered by Brandt [34] are considered to be among the most efficient acceleration techniques for the numerical solution of partial differential equations. The basic idea of the multi-grid approach is to diminish not only high but also low frequency errors efficiently through restricting the problem to coarser grids. In this work the authors use a combination of an algebraic additive correction multigrid solver with a block-ILU smoother, see Figure 1. More details on the

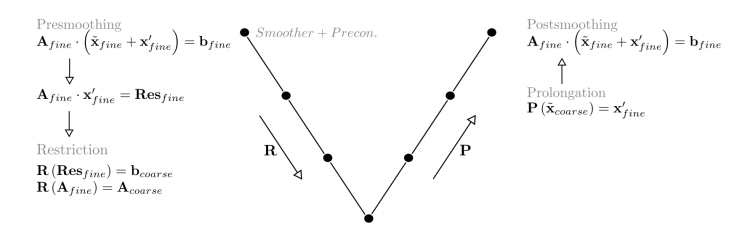


Figure 1. ADDITIVE CORRECTION MULTIGRID CYCLE WITH RESTRICTION, PROLONGATION AND PRE/POST SMOOTHING

multigrid block linear solver can be found inl [25]. Note that the multi-grid solver is also used to solver the turbulence equations even though no inter-equation coupling is accounted for in this case.

Solution Procedure

With the numerical techniques details we can now present the overall solution procedure that is used to resolve the non-linearities present in the equations Darwish [25].

- 0 Initialize values for volume flux $\dot{V}^{(n)}$, pressure $p^{(n)}$ and velocities $\mathbf{u}^{(n)}$.
- 1 Assemble source and matrix coefficients for momentum equations.
- 2 Evaluate the **D** tensor field from momentum equations' matrix coefficients.
- 3 Assemble source and matrix coefficients for continuity equation.
- 4 Solve simultaneously for pressure $p^{(n+1)}$ and velocities $\mathbf{u}^{(n+1)}$.
- 5 Solve the turbulence equations sequentially and adapt the kinematic turbulent viscosity v_t .
- 6 Extract volume flux $\dot{V}^{(n+1)}$ from continuity equation.
- 7 Return to step 1 and loop until convergence.

Results

To demonstrate the capabilities of the coupled algorithm a set of flow problems for highly compressible flows have been solved. The cases cover flow regimes from transient to fully supersonic. The accuracy and stability as well as the computational time is compared to experimental data and to results obtained with a segregated solver.

The used segregated solve is an in-house, 3D, unstructured, object-oriented finite volume code implemented into the framework of OpenFOAM[®] and designed to solve steady-state solutions of the compressible RANS-Equations [35]. The solver is based on an all-speed implementation of the SIMPLE algorithm [3].

The RMS residuals for each field are evaluated as:

$$RMS(\phi) = \frac{\sqrt{\frac{1}{N} \sum_{i=0}^{N} \left(res(\phi(i)) / a_C^{\phi\phi} \right)^2}}{max(\phi, 0) - min(\phi, 0)}$$
(24)

Circular Arc Bump The well-known transonic and supersonic flow over a circular bump [36] is used to demonstrate the accuracy and robustness of the coupled approach, see Figure 2.

For the transonic case, a single bump is considered with a thickness-to-chord ratio of 10%. While for supersonic flow two consecutive bumps are simulated with a thickness-to-chord ratio of 5%. Results are presented in terms of convergence rate and shock-capturing resolution against the numerical results of the segregated solver and data available in literature.

Transonic Flow Regime With an inlet Mach number of 0.675, the flow in the channel reaches transonic conditions over the bump. At the inlet, the flow is assumed to have uniform total pressure and temperature distribution while the direction of the flow is restricted to the normal of the face. At the outlet section, the pressure is prescribed and all other variables are extrapolated from the interior of the domain. A slip wall condition is applied at the walls. The quadrilateral grid consists of 53,000 elements.

Results are shown in Figure 3 for the Mach number contour lines along the walls. Comparison to the work of Peric [36] indicate good shock capturing behavior for the coupled solver.

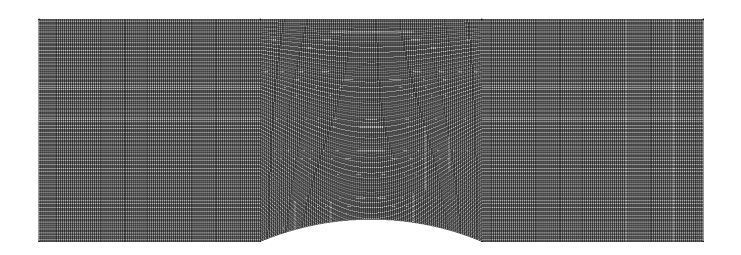
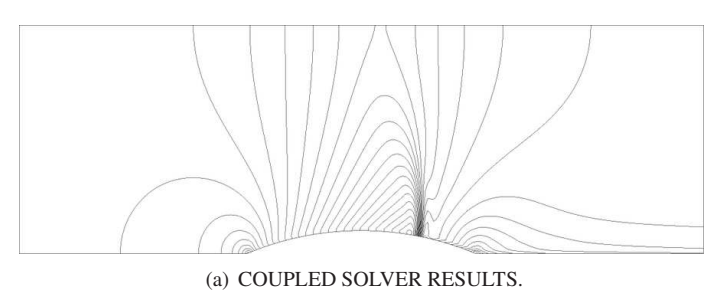


Figure 2. COMPUTATIONAL GRID FOR THE FLOW OVER A 10% ARC BUMP.



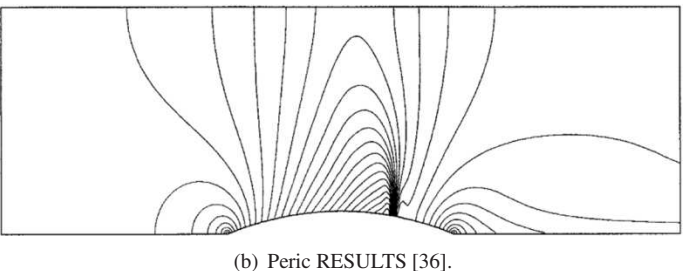


Figure 3. MACH NUMBER CONTOURS LINES.

Figure 4 shows the convergence rate residual error vs CPU times. For the coupled solver numerical simulation was stopped when the residual reached $10e^{-6}$. The figure shows an improvement

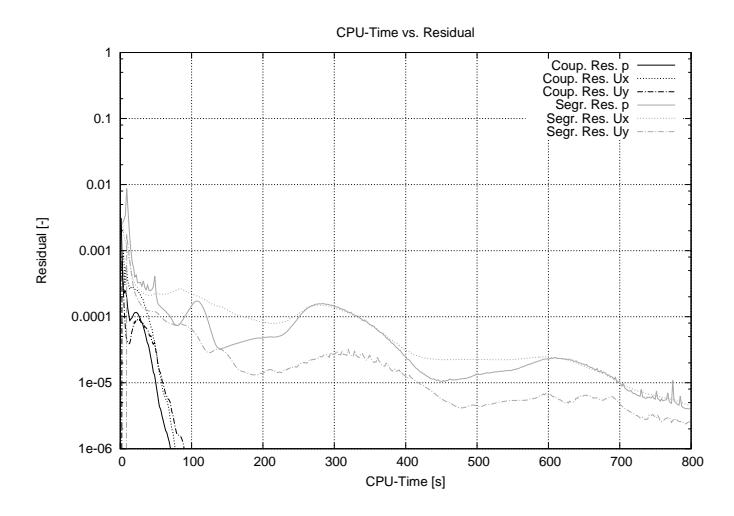


Figure 4. CONVERGENCE RATE

in computational performance of a factor of 14, in addition to increased robustness as illustrated by the smooth convergence behavior.

Supersonic Flow Regime The computational domain for the Supersonic test case is shown in Figure 5 The inlet Mach

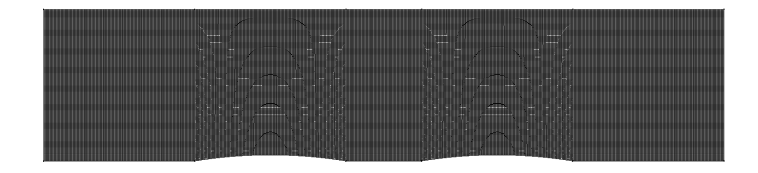


Figure 5. COMPUTATIONAL GRID FOR THE FLOW OVER A 5% BUMP.

number is set to 1.65, leading to completely supersonic flow regime in the computational domain. At the inflow domain fixed value boundary conditions are applied while for all the resolved variables extrapolation is used at the outlet. The quadrilateral grid consists of 81,000 elements.

Results are again displayed in terms of Mach number contour lines along the walls as well as in terms of convergence rate. A very sharp shocks-capturing and interaction can be seen in Figure 6. Again Figure 7 shows that the computational performance is improved by a factor of 12, along with an increase in robustness.

Stator Blade The test case is based on the experimental setup of Hylton et al. 1983 [37]. During their studies

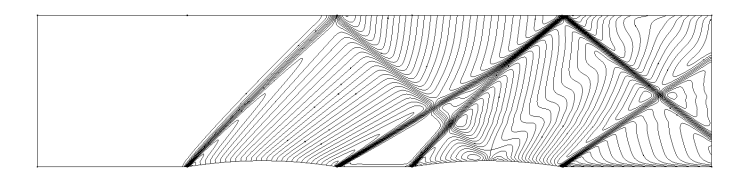


Figure 6. MACH NUMBER CONTOURS LINES.

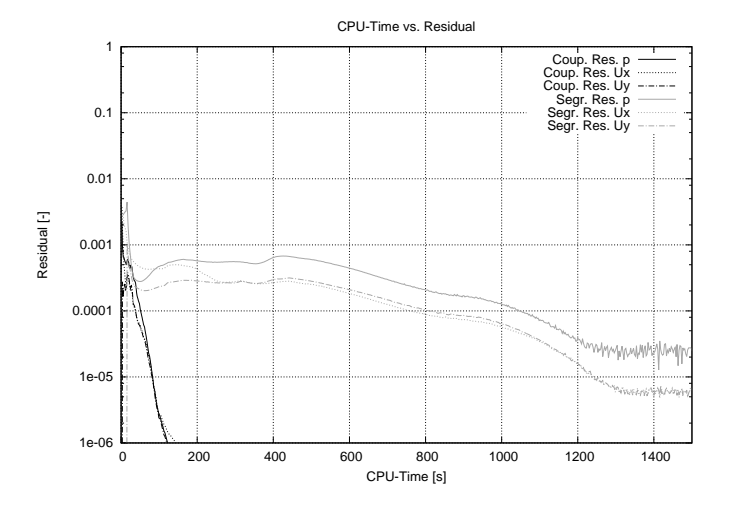


Figure 7. CONVERGENCE RATE.

they performed a detailed experimental investigation on two aero-thermodynamic linear cascade facilities. In particular the NASA-C3X cascade, made up of three vanes, was chosen as representative of a gas turbine first stage.

Periodic boundaries are used and a reduction to the usual quasi-3D domain is applied. Results obtained for one channel domain are then compared to experimental data. (Figure 8). The

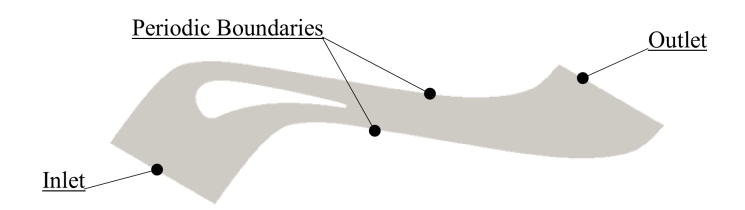


Figure 8. COMPUTATIONAL DOMAIN AND BOUNDARY CONDITIONS.

reference boundary conditions are based on a particular operating point reported by Hylton et al. 1983 (code N° 4422, run N° 112), Table 1, with an isentropic exit Mach number of 0.9.

Table 1. STATOR VANE DATA Inlet Total Pressure P_0 321800 Pa Inlet Total Temperature 783 K T_0 Dissipation Length L_d 0.001 m Tu4% Turbulence Intensity Outlet Static Pressure 192500 Pa

The computational grid was built based on O-grid type blocking, resulting with a mesh size of 14,500 hexahedral elements. Figure 9 shows that the grid fully resolves the boundary layer close to the blade walls. as well as the wake. Despite of the small mesh size, this is very demanding test case in terms of solver robustness since the very high anisotropy mesh yields element high aspect ratios up to 30,000, resulting in a stiff system of equations. Several turbulence models have been used

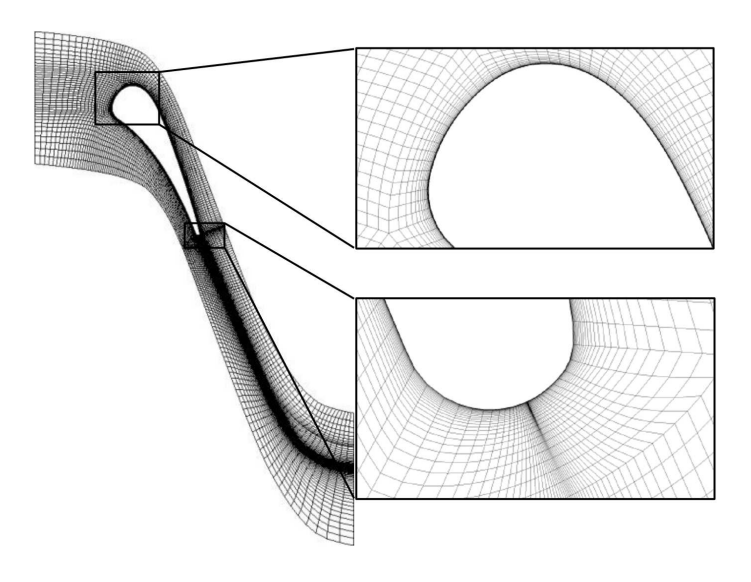


Figure 9. COMPUTATIONAL GRID.

together with the segregated solver however only results for a $k\text{-}\epsilon$ and a modified $k\text{-}\omega$ Shear Stress Transport (SST) [3] model with automatic wall treatment are presented .

Comparison using the two different turbulence models and experimental data are carried out in terms of non-dimensional pressure along axial direction normalized by the axial chord. Figure 10 shows that the blade load profile is well predicted and in good agreement with the measurement data for both the pressure and suction side of the blade. Slight differences are presents when using the k- ω model. Both the coupled and segregated solver show discrepancies near the trailing edge zone due to the downstream influence of the wake. It is worth to

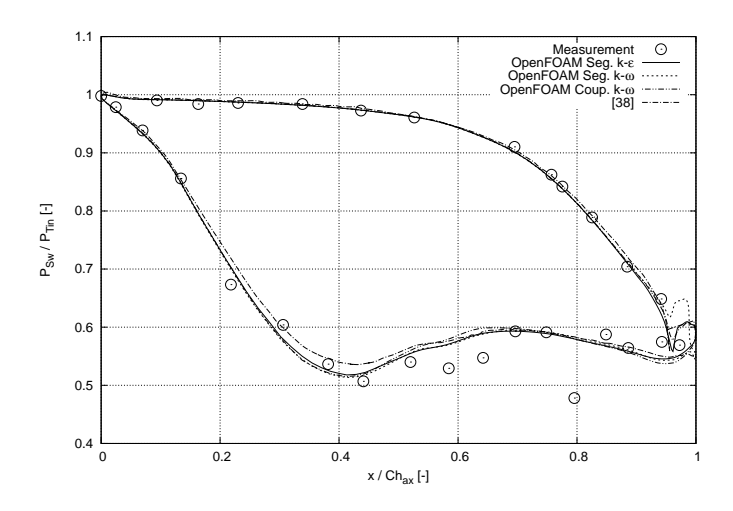


Figure 10. BLADE PRESSURE DISTRIBUTION.

	Segregated Solver	Coupled Solver	Speed Up Factor
CPU Time [s]	86	13	6.15

Table 2. COMPUTATIONAL TIME

underline that for this test case the accuracy of the predicted pressure-distribution is comparable and improved comparing with results predicted by commercial code [38].

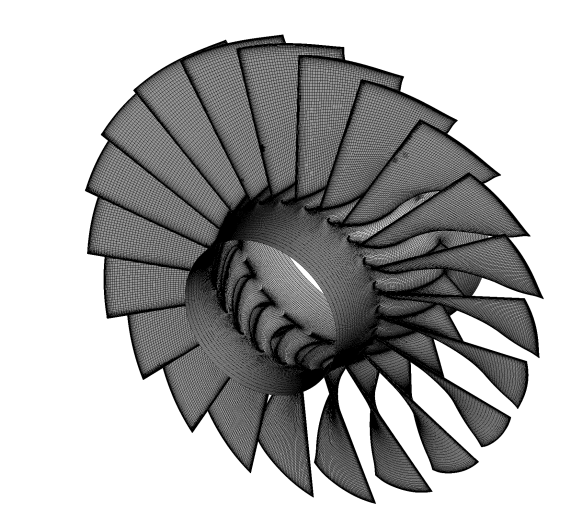
Table 2 shows the performance results for the two solvers. A reduction factor of about 6.15 is obtained, clearly demonstrating that the performance of the coupled algorithm applied also to industrial flows.

Transonic Axial Compressor Lastly the coupled algorithm was used to study the NASA rotor 67 transonic fan. The two-stage transonic fan was designed and tested with laser anemometer measurements at NASA Lewis [39]. It is a low pressure compressor, made with 22 blades. The low pressure compressor has a total of two stages and is designed for short-haul aircraft, characterized by a low aspect ratio geometry.

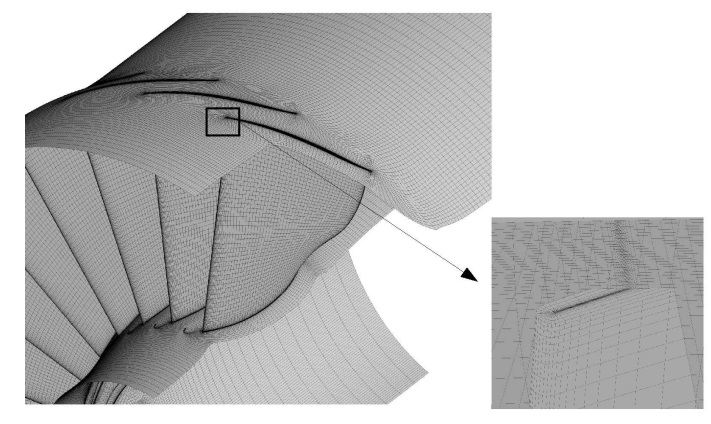
Geometry and operating conditions are listed in Table 3, with the difference that the tip clearance value has been updated by the authors accordingly to previous work [40]. A complex multi-block structure made of 700,000 elements, consisting of an O-type grid surrounding the blade and H-type grids upstream, downstream and at either side was employed in order to maximize grid quality with the tip clearance fully resolved, Figure 11. A second order spacial convection scheme was used for the steady state simulations in addition to a k- ω SST turbulence model. Total conditions were used for the inlet boundary conditions with constant flat profiles while the

Table 3. TRANSONIC AXIAL COMPRESSOR DATA

Inlet Total Pressure	P_0	101325	Pa
Inlet Total Temperature	T_0	288.15	K
Shaft Speed	n	16043	rpm
Blades Count	z	22	[-]
Choke Mass Flow Rate	ṁ	34.96	kg/s
Tip Relative Mach Number	Mr_{tip}	1.38	[-]
Design Tip Clearance	δ_{nom}	1.016 (1.1%)	mm
Modified Tip Clearance	δ	0.61	mm



(a) GRID DOMAIN.

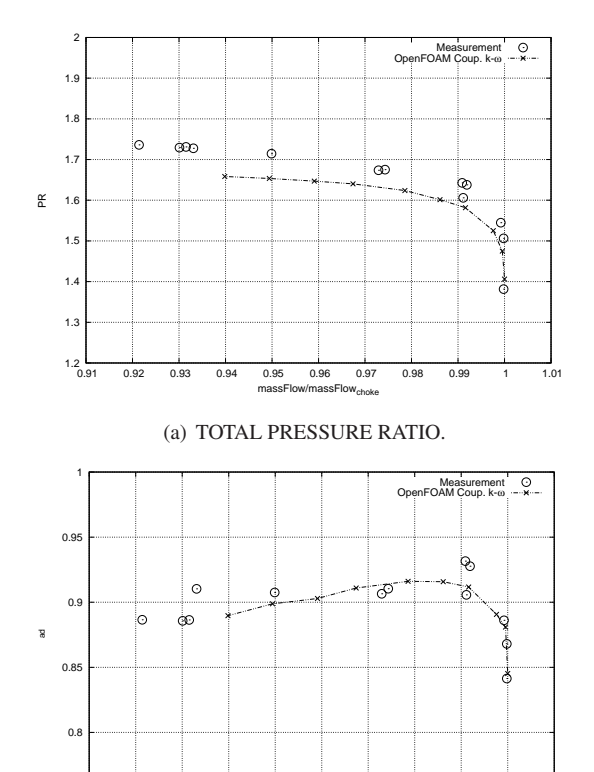


(b) TIP CLEARANCE DETAIL.

Figure 11. COMPUTATIONAL GRID.

velocity direction was kept constant and aligned with the axial direction. Calculations were executed for ten different operating points varying the outlet back pressure in order to reproduce the operating characteristics of the rotor at the design speed.

Comparisons between numerical and experimental data for the overall compressor performance was carried based on the mass flow rate normalized with the choke mass flow. Despite of the normalization process, the chocking mass flow predicted by numerical simulation, $34.62 \, kg/s$, was very accurate with a error of about 0.97% with respect to measured data. Total pressure



(b) ADIABATIC EFFICIENCY.

0.96

Figure 12. OVERALL PERFORMANCE.

ratio and adiabatic efficiency characteristics are presented. As shown in Figure 12, the overall predicted performance of the compressor is in good agreement with the experiment except for the obvious underestimated absolute total pressure ratio. The numerical results follow the same trend as the experiments, although the discrepancy slightly increases at small normalized mass flow rates. The authors investigated this phenomena finding the same underestimation also in other publications [41, 42]. It is believed that two main aspects could be investigated in order to clarify and address the problem: the distribution of the inlet boundary layer thickness (experiments also show some gradients in the inviscid core of the inlet flow) and the structural deformation not included in the present calculations. Further

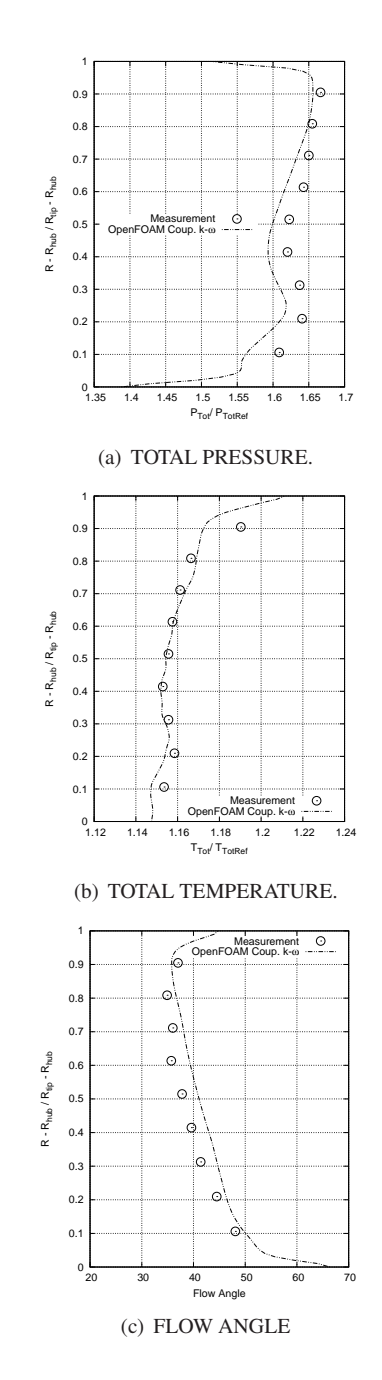


Figure 13. PEAK EFFICIENCY MASS AVERAGED PROFILES.

comparisons of the numerical results were made based on local experimental profiles and main flow features. Mass-averaged profiles of total pressure, total temperature and flow angle in a section downstream of the rotor [39], are compared in Figure 13. The predicted profiles are in good agreement respect to the experimental data. Total temperature and flow angle profiles are qualitatively and quantitatively close to the experiment, while

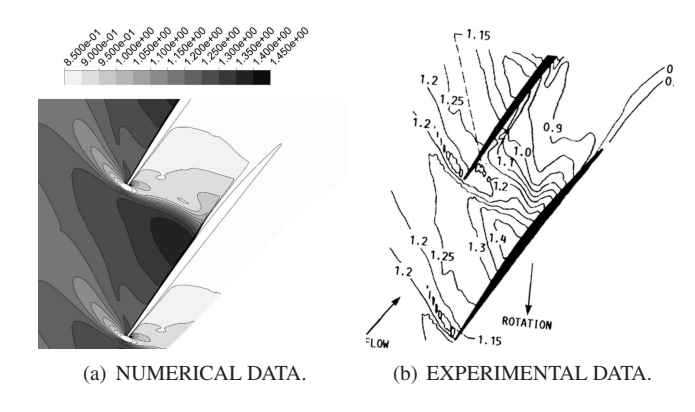


Figure 14. PEAK EFFICIENCY RELATIVE MACH NUMBERS CONTOUR PLOTS, 70% SPAN.

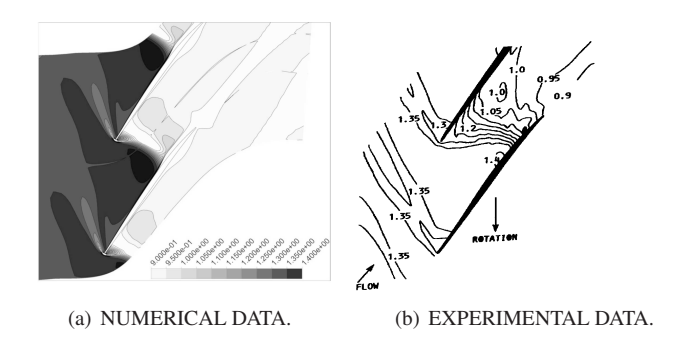


Figure 15. PEAK EFFICIENCY RELATIVE MACH NUMBERS CONTOUR PLOTS, 90% SPAN.

the total pressure, as expected, reproduce the correct shape of the profile as in the experiments but with an underestimation of the values. Based on the above statement it is clear that the uniform inlet conditions do not characterize properly the experimental setup showing the main influence close to the hub sections where a proper characterization of the inlet boundary layer seems to be fundamental. Comparisons of relative Mach number distributions in blade-to-blade sections are shown in Figures 14 and 15 at respectively 70% and 90% of the span at the peak efficiency operating point. The agreement with experiments is qualitatively good and the bow shock is not too spread out from the leading edge, showing a close correspondence with experimental data. The shock system shows the typical lambda structure formed with the leading edge bow shock, resulting in a very good agreement with measurements especially for the 70% span section as shown in Figure 14. Moreover the prediction of the passage shock structure is in line with the experiments also in terms of relative Mach number values. Downstream of the passage shock the solver predicts the separation of the turbulent boundary layer. A closer look to the numerical results and based on Schlichting evidence [43] (who stated that "turbulent boundary layers do not separate when the [static] pressure ratio P_2/P_1 is smaller than 1.8 which corresponds to Ma < 1.3 for a normal shock wave"), shows that the coupled solver is able to predict correctly the characteristic behaviour of supersonic flows and boundary layer interaction. The three dimensional effect of

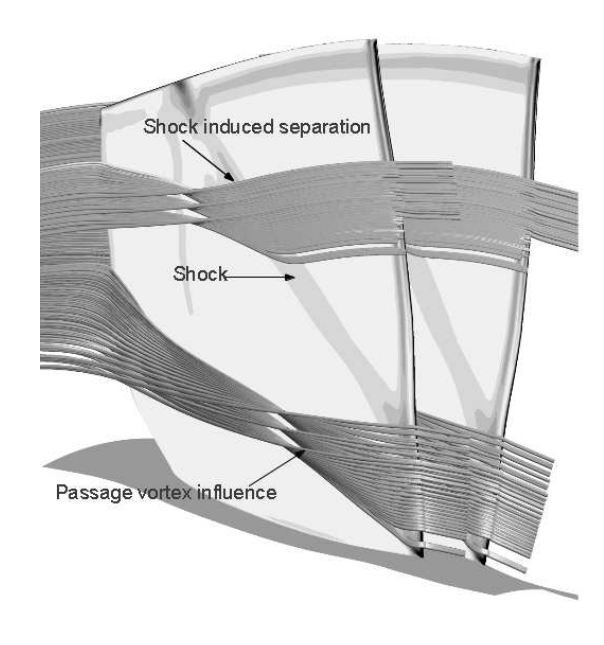


Figure 16. DENSITY GRADIENT CONTOURS AND PARTICLE TRACES CLOSE TO THE BLADE.

the passage shock is also evident in Figure 16. The passage shock induces separation on the blade suction side but only in the upper part of the airfoil where the flow lift in the radial direction is mostly related to the adverse pressure gradient and centrifugal forces. Moving the central part of the blade span the passage shock loses intensity while in the lower part of the airfoil the passage vortex is the main influence on the flow deviation.

CONCLUSIONS

In this paper a fully coupled pressure-based algorithm for the solution of turbulent compressible flows was presented. The solver was implemented in OpenFOAM® thus expending its capabilities and benefiting from its architecture.

The approach has been tested for a number of representative test cases, for flow regimes ranging from subsonic and supersonic Euler flows to fully turbulent transonic flows as well as in multiple rotating frame configuration, with three test cases representative of actual turbomachinery applications.

The results have been validated with experimental data and numerical data obtained from a well-established segregated solver.

With regard to computational performance a speedup factor in terms of CPU time of 5 to 10 was achieved for meshes up to 1'000'000 elements. For larger meshes it is expected that a higher factor would be achieved.

Future work will include larger test cases and parallel performance evaluation for a wider range of turbomachinery flow applications.

ACKNOWLEDGEMENT

The authors would like to thank Dr. Michele Marconcini of the University of Florence and Eng. Antonio Joao Ferreira Reis of the Lisbona University.

REFERENCES

- [1] Mangani, L., 2008. "Development and validation of an object oriented CFD solver for heat transfer and combustion modeling in turbomachinery application". PhD thesis, Università degli Studi di Firenze, Dipartimento di Energetica.
- [2] Di Carmine, E., Facchini, B., Mangani, L., Abba, L., Arcangeli, L., and Traverso, S., 2007. "Different manufacturing solution of fan-shaped cooling holes part II: Numerical analysis". *IGTC* 2007(ABS-54).
- [3] Mangani, L., and Andreini, A., 2008. "Application of an object-oriented CFD code to heat transfer analysis". *ASME Paper*(GT2008-5118).
- [4] Di Carmine, E., Facchini, B., and Mangani, L., 2008. "Investigation of innovative trailing edge cooling configurations with enlarged pedestals and square or semicircular ribs: Part innumerical results". ASME.
- [5] Mangani, L., Facchini, B., and Bianchini, C., 2009. "Conjugate heat transfer analysis of an internally cooled turbine blades with an object oriented cfd code". In European Turbomachinery Congress.
- [6] Mangani, L., and Maritano, M., 2010. "Conjugate heat transfer analysis of nasa c3x film cooled vane with an object-oriented CFD code". *ASME Paper*(GT2010-23458).
- [7] Mangani, L., Casartelli, E., and Mauri, S., 2011. "Assessment of various turbulence models in a high pressure ratio centrifugal compressor with an object oriented cfd code". ASME.
- [8] Mangani, L., Groschel, E., Rembold, B., and Casartelli, E., 2012. "An object-oriented CFD code for optimization of high pressure ratio compressors". ASME Turbo Expo(GT2012-68708).
- [9] Patankar, S. V., 1980. *Numerical Heat Transfer and Fluid Flow*. Taylor & Francis, US.

- [10] Patankar, S., and Spalding, D., 1972. "A calculation procedure for heat, mass and momentum transfer in three-dimensional parabolic flows". *International Journal of Heat and Mass Transfer,* 15(10), pp. 1787–1806.
- [11] Van Doormaal, J. P., and Raithby, G. D., 1984. "Enhancements of the simple method for predicting incompressible fluid flows". *Numerical Heat Transfer*, 7(2), pp. 147–163.
- [12] Issa, R. I., 1986. "Solution of the implicitly discretized fluid flow equations by operator splitting". *Journal of Computational Physics*, **62**, pp. 40–65.
- [13] Galpin, P., and Raithby, G., 1986. "Numerical solution of problems in incompressible fluid flow: treatment of the temperature-velocity coupling". *Numerical Heat Transfer, Part A: Applications,* 10(2), pp. 105–129.
- [14] Moukalled, F., and Darwish, M., 2001. "A high-resolution pressure-based algorithm for fluid flow at all speeds". *Journal of Computational Physics*, **168**(1), pp. 101–133.
- [15] Moukalled, F., and Darwish, M., 2009. "Pressure-based algorithms for single-fluid and multifluid flows". *Handbook of Numerical Heat Transfer, Second Edition*, pp. 325–367.
- [16] Pletcher, R., and Chen, K., 1993. "On solving the compressible navier-stokes equations for unsteady flows at very low mach numbers". In AIAA 11th Computational Fluid Dynamics Conference, Vol. 1, pp. 765–775.
- [17] Karki, K. C., and Patankar, S. V., 1989. "Pressure based calculation procedure for viscous flows at all speeds in arbitrary configurations". *AIAA Journal*, **27**(9), pp. 1167–1174.
- [18] Darwish, M., Moukalled, F., and Sekar, B., 2001. "A unified formulation of the segregated class of algorithms for multifluid flow at all speeds". *Numerical Heat Transfer: Part B: Fundamentals,* **40**(2), pp. 99–137.
- [19] Darwish, M., Sraj, I., and Moukalled, F., 2009. "A coupled finite volume solver for the solution of incompressible flows on unstructured grids". *Journal of Computational Physics*, **228**(1), pp. 180–201.
- [20] Turkel, E., 1999. "Preconditioning techniques in computational fluid dynamics". *Annual Review of Fluid Mechanics*, *31*(1), pp. 385–416.
- [21] Caretto, L., Gosman, A., and Spalding, D., 1971. "Removal of an instability in a free convection problem". In Conference on Applications of Numerical Analysis, Springer, pp. 264–269.
- [22] Benzi, M., Golub, G., and Liesen, J., 2005. "Numerical solution of saddle point problems". *International Journal for Numerical Methods in Fluids: Acta numerica,* 14(1), pp. 1–137.
- [23] Patankar, S., 1980. *Numerical Heat Transfer and Fluid Flow*. Hemisphere Publishing, Washigton.
- [24] Rhie, C., and Chow, W., 1983. "A numerical study of turbulent flow past an isolated airfoil with trailing edge

- separation". AIAA Journal.
- [25] Darwish, M., Sraj, I., and Moukalled, F., 2008. "A coupled finite volume solver for the solution of incompressible flows on unstructured grids". *Journal of Computational Physics*.
- [26] Muzaferija, S., 1994. "Adaptive finite volume method for flow predictions using unstructured meshes and multigrid approach". PhD thesis, University of London.
- [27] Ferziger, J., and Peric, M., 1994. *Computational Methods for Fluid Dynamics*. Springer, Berlin.
- [28] Jameson, A., and Yoon, S., 1985. "Multigrid solution of the euler equations using implicit schemes". In 23th AIAA Sciences meetings.
- [29] Roe, P. L., 1981. "Approximate riemann solvers, parameter vectors and difference schemes". *Journal of Computational Physics*, 43, pp. 357–372.
- [30] Jasak, H., Weller, H. G., and Gosman, A. D., 1999. "High resolution nvd differencing scheme for arbitrarily unstructured meshes". *International Journal of Numerical Methods in Fluids*, *31*, pp. 431–449.
- [31] Hirsch, C., 1991. Numerical Computation of Internal and External Flows. Wiley, NY.
- [32] Federenko, R., 1962. "A relaxation method for solving elliptic difference equations". USSR Computational Mathematics and Mathematical Physics.
- [33] Poussin, F., 1968. "An accelerated relaxation algorithm for iterative solution of elliptic methods". *SIAM Journal of Numericla Analysis*.
- [34] Brandt, A., 1977. "Multi-level adaptive solutions to boundary value problems". *Mathematics of Computation*.
- [35] Mangani, L., Bianchini, C., Andreini, A., and Facchini, B., 2007. "Development and validation of a c++ object oriented CFD code for heat transfer analysis". ASME Summer Heat Transfer (AJ-1266).
- [36] Peric, M., Lilek, Z., and Demirdzic, L., 1993. "A collocated finite volume method for predicting flows at all speed". *Journal of Numerical Methods in Fluids*, 16, pp. 1029–1050.
- [37] Hylton, L. D., Mihelc, M. S., Turner, E. R., Nealy, D. A., and York, R. E., 1983. Analytical and experimental evaluation of the heat transfer distribution over the surfaces of turbine vanes. Tech. Rep. 182133, NASA, Lewis Research Center, Cleveland Ohio.
- [38] Facchini, B., Magi, A., and del Greco, A. S., 2004. "Conjugate heat transfer simulation of a radially cooled gas turbine vane". In Proceedings of ASME Turbo Expo, no. GT2004-54213.
- [39] Strazisar, A. J., Wood, J., and Suder, K. L., 1989. Laser anemometer measurements in a transonic axial-flow fan rotor. Tech. Rep. 2879, NASA, Lewis Research Center, Cleveland Ohio.
- [40] Grosvenor, A. D., 2007. "Rans prediction of transonic

- compressive rotor performance near stall". *ASME Paper*(GT2007-27691).
- [41] Du, J., Lin, F., Zhang, H., and Chen, J., 2008. "Numerical investigation on the originating mechanism of unsteadiness in tip leakage flow for a transonic fan rotor". In Trans. ASME, ASME Paper GT2008-51463.
- [42] Doi, H., and Alonso, J., 2002. "Fluid/structure coupled aeroelastic computations for transonic flows in turbomachinery". In Trans. ASME, ASME Paper GT2002-30313.
- [43] Schlichting, H., 1960. *Boundary Layer Theory*. McGraw-Hill.